The NCAR–NOAA Global Hawk Dropsonde System

Gary A. Wick,[a] Terrence F. Hock,[b] Paul J. Neiman,[a] Holger Vömel,[b]
Michael L. Black,[c,e] and J. Ryan Spackman[d]

[a] *Physical Sciences Division, NOAA/Earth System Research Laboratory, Boulder, Colorado*
[b] *Earth Observing Laboratory, National Center for Atmospheric Research, Boulder, Colorado*
[c] *Hurricane Research Division, NOAA/Atlantic Oceanographic and Meteorological Laboratory, Miami, Florida*
[d] *Earth Science Division, NASA Ames Research Center, Moffett Field, California*

(Manuscript received 28 December 2017, in final form 9 April 2018)

ABSTRACT

A new remotely controlled Airborne Vertical Atmospheric Profiling System (AVAPS) dropsonde system has been developed for and deployed on the NASA Global Hawk (GH) unmanned aircraft. Design, fabrication, and operation of the system was led by the National Center for Atmospheric Research (NCAR) with support from the National Oceanic and Atmospheric Administration (NOAA) Unmanned Aircraft Systems (UAS) Program. The system has employed the NCAR Research Dropsonde 94 (NRD94) dropsonde, a smaller and lighter version of the standard RD94 dropsonde deployed from manned aircraft but with virtually identical sensors. The dropsondes provide in situ atmospheric profiles of temperature, pressure, and humidity at a 2-Hz data rate, and wind speed and direction at 4 Hz. The system is capable of carrying up to 90 dropsondes and can support eight simultaneous soundings. Operation from the GH means that the dropsondes can be deployed from altitudes up to 19.8 km during flights in excess of 24-h duration. The dropsonde launch is commanded directly by an operator on the ground in coordination with the aircraft commander. Over 2700 total dropsondes have been deployed from the GH during four major campaigns since 2011. Data are processed in near–real time and have been employed by forecasters, for assimilation in numerical weather prediction models, and in diverse research studies. Intercomparison studies suggest the performance of the GH NRD94 dropsondes is similar to those deployed from manned aircraft. This paper describes the components and operation of the system and illustrates its unique capabilities through highlights of data application to research on the Arctic atmosphere, atmospheric rivers, and tropical cyclones.

1. Introduction

Detailed measurements of the kinematic and thermodynamic structure of the atmosphere are important for numerical weather prediction (NWP) and physical process studies. While satelliteborne microwave and infrared sounders retrieve global thermodynamic profiles at relatively coarse vertical resolution, radiosondes and dropsondes (also called dropwindsondes) provide high-quality high-vertical-resolution in situ measurements of atmospheric wind, temperature, and relative humidity (RH). Assimilating these observations into weather forecast models typically has a positive impact on the forecasts as quantified by multiple metrics. Of all the assimilated data, observations from the Advanced Microwave Sounding

Unit (AMSU) commonly have the largest total impact on forecasts with radiosondes ranking very high and, when available, dropsondes are often found to have the greatest or near-greatest impact on a per-observation basis (e.g., Ota et al. 2013; Gelaro et al. 2010). For high-vertical-resolution atmospheric profile measurements over the oceans, particularly in stormy environments, dropsondes are the most widely employed observing system. Operational programs for collecting dropsonde measurements for hurricane surveillance in support of forecasting are conducted within the United States by the National Oceanic and Atmospheric Administration (NOAA) and the U.S. Air Force. Beyond their forecast value, the utility of the dropsonde observations for research studies of hurricanes (e.g., Franklin et al. 2003; Braun et al. 2016), and atmospheric rivers (ARs; e.g., Ralph et al. 2011), among other things, is well documented.

Dropsonde technology has advanced significantly over the years, and the number and range of platforms from

---

[e] Deceased.

Corresponding author: Gary A. Wick, gary.a.wick@noaa.gov

which they are deployed have grown. Many of the main improvements have been related to the method by which wind speed and direction are inferred. Dropsondes developed at the National Center for Atmospheric Research (NCAR) evolved from the omega-based dropwindsonde in the early 1970s (Cole et al. 1973) to the lightweight long-range navigation (loran) digital dropwindsonde (Hock and Cole 1991), and then to the current global positioning system (GPS)-based dropsonde (Hock and Franklin 1999). The GPS dropsonde system is now named the Airborne Vertical Atmospheric Profiling System (AVAPS) dropsonde system. The history of dropsonde development is described in more detail by Hock and Franklin (1999).

The NCAR AVAPS dropsonde system has been deployed in different forms on multiple platforms to satisfy varied requirements and capabilities. It has been deployed operationally within the United States on the NOAA WP-3Ds and Gulfstream IV-SP (G-IV), and the Air Force 53rd Weather Reconnaissance Squadron WC-130Js; for research applications on National Science Foundation (NSF) and National Aeronautics and Space Administration (NASA) traditional manned aircraft; and internationally on aircraft from Germany, the United Kingdom, and Taiwan. More recently, a balloonborne driftsonde system (Cohn et al. 2013) was developed to enhance deployment opportunities in very remote locations such as over the middle of the oceans or the interior of Antarctica. Development of the driftsonde system also corresponded with the introduction of a smaller and lighter version of the GPS dropsondes termed the Miniature In-Situ Sounding Technology (MIST) dropsonde (Cohn et al. 2013).

Another deployment opportunity with tremendous potential arose with the acquisition of Global Hawk (RQ-4A) unmanned aircraft by NASA. The Northrop Grumman Global Hawk (GH) is a high-altitude, long-endurance unmanned aircraft with a single turbofan jet engine. Detailed physical and performance specifications of the GH are listed in Table 1. The GH typically climbs rapidly to an altitude around 17 400 m and then enters a cruise climb mode where it slowly continues to climb to above 18 300 m as it burns off fuel. Science missions are commonly designed for 24–26-h duration, corresponding to a range in excess of 14 000 km.

NASA initially operated two of the original preproduction GH aircraft. They have since obtained several of the ''Block 10'' first-generation production aircraft from the U.S. Air Force and are currently modifying one of those to replace the preproduction aircraft. The first science mission of the NASA GH was the Global Hawk Pacific (GloPac) Mission, conducted in 2010, and its subsequent usage has included several campaigns focused on weather and atmospheric composition (e.g., Braun et al. 2013; Braun et al. 2016; Jensen et al. 2017; Dunion

TABLE 1. Global Hawk specifications and capabilities.

Physical specifications	
Length	13.5 m (44.4 ft)
Wingspan	35.4 m (116.2 ft)
Height	4.6 m (15.2 ft)
Performance characteristics	
Endurance	31+ h
Payload	>681 kg (1500 lb)
Maximum altitude	19 800 m (65 000 ft)
Ground speed	$\sim$172 m s^{-1} (335 kt)

et al. 2018). The aircraft enables advances in atmospheric research through its combination of exceptional endurance, payload capacity, and high flight altitudes. A GH-based dropsonde system permits targeted deployment of large numbers of sondes from high, stratospheric altitudes, safely above significant weather events, sampling more vertical extent of the atmosphere than traditional manned aircraft while covering large geographic regions and/or an extended period as weather features evolve.

To capitalize on this potential new capability, the Earth Observing Laboratory (EOL) at NCAR developed a new automated dropsonde system, based on its well-established AVAPS dropsonde technology, for the NASA GH with support from the NOAA Unmanned Aircraft Systems (UAS) Program. This paper describes this GH dropsonde system, its operation, and highlights results from its deployments to date.

2. Global Hawk dropsonde system description

Development of a dropsonde system for remote operation on the GH posed many design challenges for both the deployment system and the sondes. Potential installation locations were limited in number, unpressurized, and were subject to volume and access constraints, as well as very cold ambient temperatures in flight. Moreover, the long endurance of the aircraft required that the dropsondes be stored in unfavorable conditions for extended periods of time and then be initialized remotely. Satisfying the aircraft constraints and requirements for remote, automated GH operation required development of an entirely new launcher system and significant upgrades to the AVAPS software. The GH AVAPS dropsonde system is composed of two primary components—the launcher assembly and the data system—installed in different locations on the aircraft. The remainder of this section details the GH dropsondes and the individual components of the dropsonde system.

a. Dropsondes

The GH dropsondes are a smaller, lighter version of the sondes currently deployed from manned aircraft, but
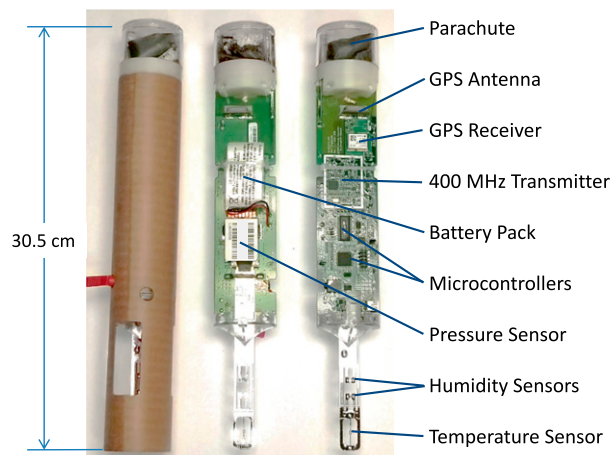
FIG. 1. Photograph of the NRD94 dropsonde utilized in the GH dropsonde system with key components highlighted. (Photo copyright University Corporation for Atmospheric Research; used with permission.)

TABLE 2. Global Hawk dropsonde specifications.

Physical specifications			
Weight	167 g		
Length	30.5 cm		
Diameter	4.6 cm		

Sensor specifications			
	Range	Resolution	Repeatability[a]
Pressure	1080–3 hPa	0.1 hPa	0.4 hPa
Temperature	$-90°$ to $+60°C$	$0.1°C$	$0.2°C$
Humidity	0%–100%	1%	2%
Wind speed	$0–100 \, m \, s^{-1}$	$0.1 \, m \, s^{-1}$	$0.2 \, m \, s^{-1}$

[a] Standard deviation of differences between two successive repeated calibrations.

the sensor components are virtually the same. The sondes utilized from system inception through 2017 were termed the NCAR Research Dropsonde (NRD) 94 sondes. These are a further evolution of the NCAR MIST sondes described by Cohn et al. (2013). A photograph of a GH dropsonde is shown in Fig. 1, illustrating the sensors and primary components. The physical and sensor specifications are documented in Table 2. As of this writing, a new version with the same form factor and functionality is being finalized based on the newest generation of sensor module from Vaisala. The new module includes a faster response temperature sensor and an improved humidity sensor.

The NRD94 dropsondes incorporated the Vaisala RSS904 sensor module, which is the same as that utilized in the NCAR-licensed Vaisala RD94 dropsonde deployed from manned aircraft and is similar to that used in the standard Vaisala RS92-SGP radiosonde. The module includes a THERMOCAP capacitive bead temperature sensor, a BAROCAP silicon pressure sensor, and an H-HUMICAP thin-film capacitor for measurement of relative humidity (Vaisala 2016). Each sensor is initially calibrated with traceability to international standards at Vaisala and subsequently verified at NCAR during sonde production. Wind speed and direction are derived from GPS measurements obtained with a u-blox NEO series receiver module. Pressure, temperature, and humidity (PTU) measurements are collected continuously at 2 Hz and wind speed and direction are sampled at 4 Hz during the sonde's descent from the aircraft.

Physical assembly of the GH dropsondes is completed by NCAR. The Vaisala sensor and u-blox GPS modules are attached to an electronic circuit board along with an

8-V lithium battery pack, a microprocessor, 100-mW 400-MHz telemetry transmitter, UHF and GPS antennas, and other electronics, and enclosed in a phenolic cardboard tube. There is also a connector that enables sonde testing and humidity sensor reconditioning prior to loading, and a receptacle for a power pin that disconnects the battery from the electronics. The UHF antenna also functions as a spring to help open the parachute cap during the launch sequence.

The parachute employs a square-cone design that is optimized for stable dropsonde descent and high-accuracy wind measurements. The design is the same as that used on the RD94 dropsondes but the size is smaller (20 cm on a side) to correspond to the weight of the GH dropsonde and result in a similar fall speed ($\sim11 \, m \, s^{-1}$ at the surface, corresponding to a vertical resolution of $\sim6 \, m$ for the PTU measurements and 3 m for wind).

Beyond reduced size and weight, modifications of the GH dropsondes addressed the need for remote initialization following extended storage. The 24+ hour endurance of the GH coupled with potential aircraft preflight preparations the day before takeoff means that there can be periods approaching 48 h between the time a sonde is prepared for loading in the aircraft and its actual deployment. Once the power pin is removed and self-tests are completed, the sondes enter an ultralow power mode where they can remain for 2–3 weeks. The sondes contain an added infrared communication device via which the sondes are awoken and initialized prior to launch, including assignment of their specific transmission frequency.

Previous estimates of the accuracy of the larger RD94 dropsonde measurements under actual sampling conditions were presented by Hock and Franklin (1999). Given the similarity of the sensor modules and descent characteristics, the accuracy of the measurements from the GH dropsondes is expected to be consistent (generally confirmed by two dedicated intercomparisons between nearly coincident dropsondes deployed from the GH and the NOAA G-IV; see section 4b). A dry bias affecting the
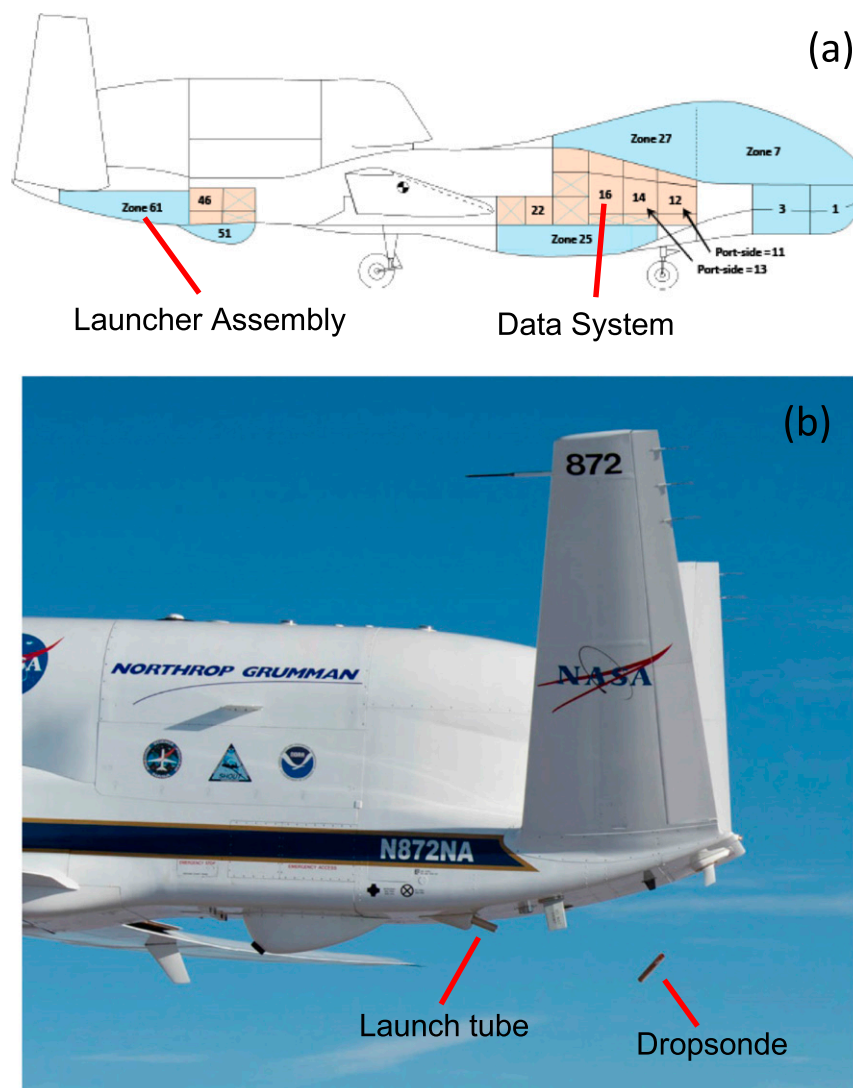
FIG. 2. (a) Schematic illustrating integration location of the dropsonde system components in the GH payload zones. (b) Photograph of a dropsonde being deployed from the NASA GH during system testing over Edwards AFB. The launch tube is visible, extending from the aft lower side of the aircraft, and the dropsonde can be seen in the air behind. (GH schematic and photograph courtesy of NASA and used with permission.)

initial measurements from both the RD94 and NRD94 sondes at temperatures below approximately −10°C prior to April 2016 was recently identified (Vömel et al. 2016) and a correction has been implemented. A more comprehensive evaluation of the accuracy and reliability of the dropsonde measurements is currently in preparation.

b. Launcher assembly

The launcher assembly of the GH AVAPS dropsonde system is installed in zone 61 at the rear underside of the GH fuselage (Fig. 2a), thus facilitating a clean separation of the sonde from the aircraft. A photograph further

illustrating the installation location and capturing a successful launch is shown in Fig. 2b. Use of this location also frees the primary payload bays on the aircraft for other instruments, enhancing mission compatibility. The ~46-kg assembly is composed of four primary components: the sonde storage box, a carriage to move the sondes to the launch tube, the ejection unit, and an electronics control box. A photograph of the assembly mounted on a test stand is shown in Fig. 3.

The sonde storage box contains 10 vertical columns into which up to 90 sondes are loaded. To prevent the sondes from becoming too cold during the flights and to
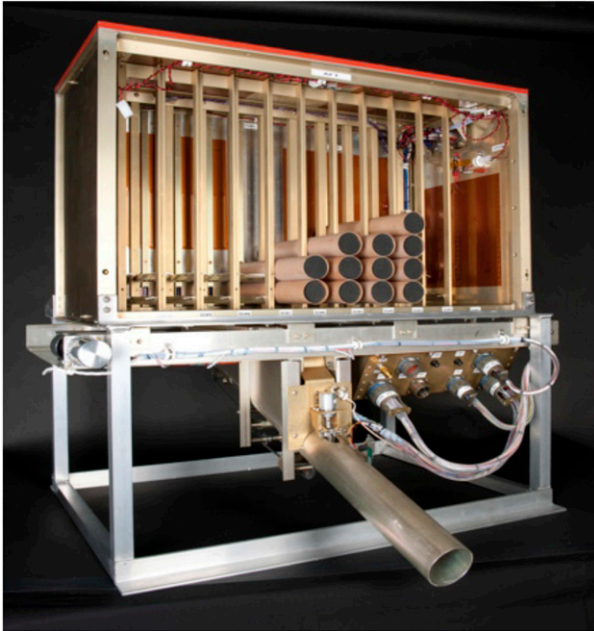
FIG. 3. Photograph of the GH dropsonde system launcher assembly mounted on a test stand. (Photograph courtesy of NCAR EOL.)

improve system reliability in the harsh environment, contact film heaters are installed on the inside walls of the box. Two sets of latches are incorporated into each column to drop sondes individually into the carriage below. One latch holds the lowermost sonde in place, while the second latch is aligned just above this sonde and holds the remaining sondes above. Release of each latch is activated through a solenoid and pin. When the solenoid is activated, a pin holding the latch in place is retracted and the sondes drop under the force of gravity. The latches are spring loaded such that they swing back into the closed position and the pins extend again to lock them in place. During a load sequence, the lowest latch is activated first, allowing the lowermost sonde to drop into the carriage. The second latch is then released after the first has returned to its closed position and the remaining sondes drop down onto the lowest latch. The second latch returns to its closed position above the lowest sonde, securing any remaining sondes above. Optical proximity sensors are aligned in each bin to detect whether sondes are available.

The carriage assembly installs below the storage box and transfers sondes into the launch tube. The unit primarily consists of a carriage, motor, and drive chain. During the load sequence, the carriage is positioned under the desired column of the storage box and a single sonde is dropped into it. The carriage is then moved over the ejection assembly via the chain drive and the sonde drops through an opening in the base into the launch tube.

Accurate positioning of the carriage beneath the storage column is important so that the sonde falls freely into the carriage and the latch closes securely behind the sonde.

The sonde ejection assembly includes the launch tube, ejection motor, shuttle, safety latch unit, and sonde infrared wireless communication module. The upper half of the launch tube is open inside the aircraft but enclosed aft of the safety latch where it extends outside the aircraft. The shuttle, which physically makes contact with the sonde and forces it out of the aircraft, is mounted through a channel in the base of the launch tube to a drive chain that is connected to the ejection motor. The ejection motor was selected for its ability to accelerate rapidly and to function at cold temperatures. A contact heater is affixed to its surface to further assure its reliable performance. The infrared communication assembly enables power-on and initialization of the sonde once it is in the launch tube. The safety latch mechanism ensures there is no unintended dropsonde release. A latch, held in place with a holding brake, blocks a sonde from exiting the launch tube until it is released. The assembly is connected to a safety interlock relay controlled by the GH mission director. The release of sondes from the GH is regulated by air traffic control agencies and is the responsibility of the pilot in charge. Operation of the safety latch and power to the ejection motor is disabled via the interlock until the pilots deem the aircraft is in a safe location for sonde deployment.

The electronics control box, mounted under the carriage assembly to the side of the ejection assembly, controls operation of the launcher as commanded by the data system. In addition to controlling all the latches, carriage motor, and shuttle motor, it monitors all aspects of the launcher, including positions of moving components, dc power supplies, currents, and temperatures throughout the launcher assembly. The unit interfaces to the GH experimenter interface panels (EIP) for power and Ethernet communications to the data system.

c. Data system

The ~26-kg data system assembly includes the onboard computer, an uninterruptable power supply, the telemetry chassis, and an interface unit for connecting to the aircraft's EIP. A compact dedicated spectrum analyzer has been added to characterize any potential electromagnetic interference on the aircraft. The individual components are mounted on a pallet and installed in zone 16, which is located on the forward starboard side of the aircraft (Fig. 2a). Photographs identifying the components are shown in Fig. 4.

The onboard computer is a small ruggedized unit designed for operation in harsh environments. Communications with the launcher assembly is via the aircraft
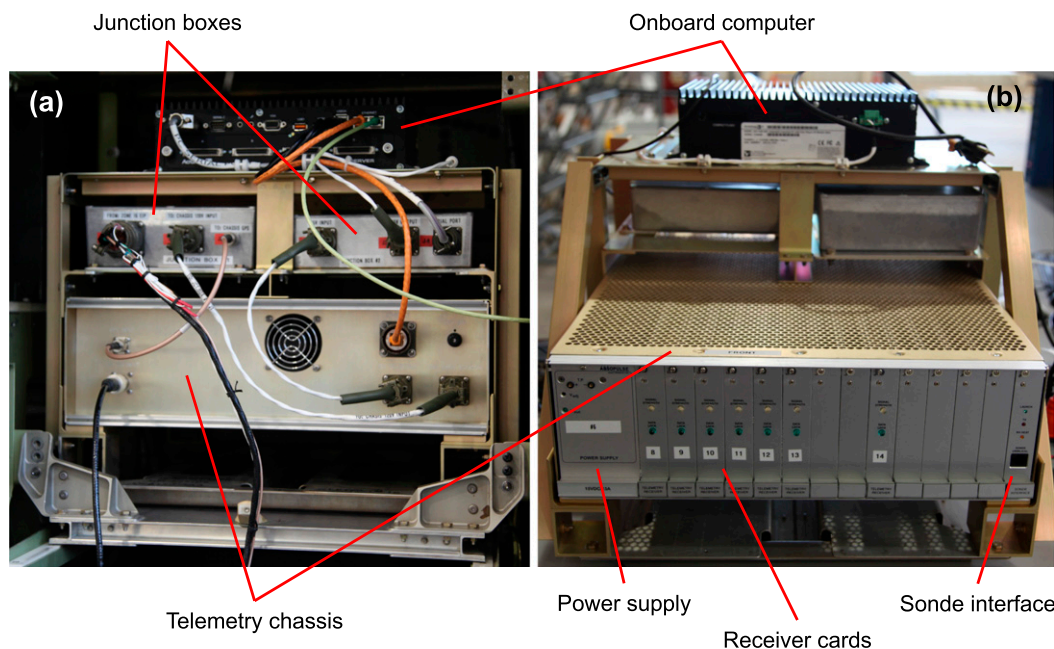
FIG. 4. Photographs of the data system with key components highlighted. (a) The system as installed and visible inside the aircraft and (b) the back of the assembly, better illustrating the components of the telemetry chassis (photographs by G. Wick).

Ethernet, while communication with the telemetry chassis uses a direct Ethernet interface. The computer also communicates with the aircraft's data system and the ground via the aircraft network. The aircraft's data system enables input of aircraft state parameters, such as pressure, temperature, and altitude, and facilitates transmission of the collected sounding data. Remote login into the dropsonde system computer is possible from the ground.

The telemetry system includes eight channels to independently receive and process data from eight sondes simultaneously. Configuration and components of the system closely resemble that of AVAPS installations on traditional manned aircraft. The telemetry chassis is composed of a power supply card, a dropsonde interface card, nine narrowband 400-MHz telemetry receiver cards, and a reference GPS receiver. Eight receivers process the 400-MHz radio frequency (RF) signal and demodulate the sonde PTU and GPS data for each channel, while the ninth records engineering data, such as receiver strength, for all of the deployed sondes. The interface card works with the AVAPS computer to communicate with the sondes and to assign the transmitter frequency.

The system operation uses a special version of the NCAR AVAPS software designed for automated launchers and remote operation. The AVAPS software is run under Laboratory Virtual Instrument Engineering Workbench (LabVIEW) on the onboard computer and controls the entire dropsonde system operation

and sounding file creation on the aircraft. Modifications to the system for GH operation include the addition of an interface to new ground control software (see section 3), launcher control, and automated frequency selection for the dropsondes. The system continuously scans the meteorological 400–406-MHz spectrum to automatically select the center frequency with the lowest background noise level for each sonde to minimize RF interference from other signals. The selection of the transmitter frequency can be configured to be from the entire 400–406-MHz range or one of five blocks composed of six 200-kHz subbands to prevent signal overlap with adjacent dropsonde deployments from other aircraft during coordinated flights.

3. GH AVAPS dropsonde system operation

Operation of the GH AVAPS dropsonde system includes sonde deployment, real-time quality control (QC) of the completed soundings, and operational transmission of the resulting data to enable assimilation by NWP models and analysis by forecasters and scientists. Control of the system is carried out by an operator on the ground in the GH payload operations room in communication with the mission director and pilots. The launch of each dropsonde is commanded directly from the ground, facilitating real-time modifications to the planned flight track and drop locations, and deconfliction with other

aircraft. The system was designed to function using both the low data bandwidth Iridium and high data bandwidth Ku-band satellite systems employed on the NASA GH.

Prior to flight every sonde is tested and prepared for operation. Checks ensure the PTU and GPS modules are functioning and the battery voltage is within specification. As part of the preflight checks, the humidity sensors are "reconditioned" in a procedure in which they are heated to remove possible contamination. Loading of the sondes can occur up to a day before the flight.

Ground control and monitoring of the dropsonde system is performed using the AVAPS Ground Software (AGS) developed by NCAR specifically for remote AVAPS operations. Fundamentally, the operation of the system is controlled by two buttons: one to load a sonde and a second to launch the sonde. The AGS provides these functions along with an interface to monitor real-time data from the sondes, to monitor the health of the system, and to enable individual system component commands by an experienced operator. Screenshots from two of the six display tabs are displayed in Fig. 5.

The first tab (Fig. 5a) allows control of the system while viewing a graphical display of real-time sonde data. The top of this screen (and all others) has the load and launch buttons along with several indicators displaying high-level system status. The load and launch buttons are enabled only if health indicators and system logic determine that the operation is safely possible. Loading is allowed only if a sonde is available in the dispenser and a telemetry channel is free. Once the load command is issued by clicking on the button, successive indicators are illuminated as the sonde is transferred to the launch tube and initialized. The initialization process includes waking the sonde, testing the battery and PTU units, and establishing GPS communications with available satellites through the coupling of a low-level GPS signal. Because of the serial nature of the launcher, a sonde must be physically ejected from the launcher before another can be loaded, even if the sonde does not pass all tests. When the sonde is loaded, initialized, and the pilot interlock disabled, the launch button turns green and the sonde is launched by clicking on the button. Following launch, the plots below show real-time vertical profiles of the data for each channel. Color coding indicates whether the channels are currently active. A second (sounding) tab (not shown) shows the data from active sondes in a scrolling tabular format.

The status/maintenance tab (Fig. 5b) includes several additional status indicators useful for monitoring the health and operation of the system in the top half of the display and an interface for issuing manual system commands at the bottom. The indicators display such things as sonde availability in the different bins, telemetry channel status, and progress through the various

steps associated with loading and initializing the sondes. Manual commands can be input at the bottom of the screen to individually control subcomponents of the launcher and data systems to perform specific tasks, to override automatic operation, or to troubleshoot problems. Additional tabs (not shown) display detailed engineering data from system components, a record of messages sent to and from the system, and a log of launches.

The achievable launch frequency is a function of system constraints and mission objectives. The load and initialization process typically takes less than 60 s. Rapid launch sequences are possible by loading a new sonde as soon as the previous sonde is launched. Successive launches with as little as 60-s ($\sim$10 km) separation have been demonstrated, though the limitation of eight active soundings can limit sustained rapid launches. For the available channels and typical sonde descent time ($\sim$20 min), the maximum sustained deployment rate is about one every 3 min, which corresponds to a spacing of $\sim$30 km.

The complete data flow through real-time processing and distribution is illustrated in Fig. 6. System commands are relayed to the aircraft and status messages are returned through both Iridium and high-rate Ku-band satellite communications, if available. Following launch, all sonde sensor and engineering data are radioed back to the aircraft. These data are relayed to the ground from the aircraft in real time over Iridium and Ku band for display within AGS, but they can be subject to dropouts in the satellite communications. Following completion of the sounding, a standard AVAPS "D" raw sounding file is constructed by the AVAPS computer on board the aircraft and transmitted to the ground over the Ku-band communications. This file is received by a NASA ground computer (the link server) and scripts push the file to NOAA computers, where the data are available for near-real-time QC.

Real-time QC of the data is performed by scientists using the Atmospheric Sounding Processing Environment (ASPEN) software developed by NCAR. This software applies several automated QC algorithms, including nearest-neighbor comparisons. ASPEN also constructs graphics, World Meteorological Organization (WMO) formatted data files for ingestion to NWP models, and full-resolution data files for research applications. While automated execution is possible, interactive application of the software is preferred to enable assessment of important factors like whether the sonde successfully transmitted all the way to the surface. Careful QC is critical given the potential impact of the data on data assimilation systems. The WMO files are submitted in near–real time through the Global Telecommunication System (GTS) for operational model access, and the graphics and full-resolution data are made available for research access
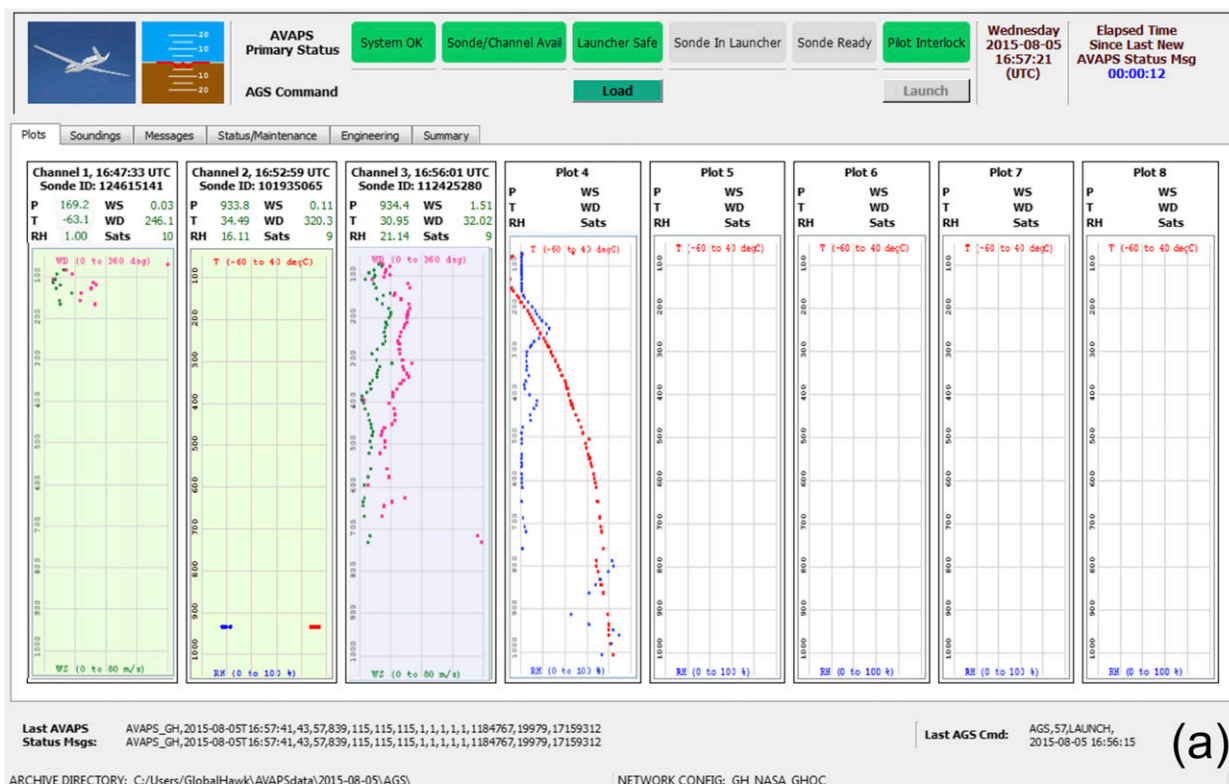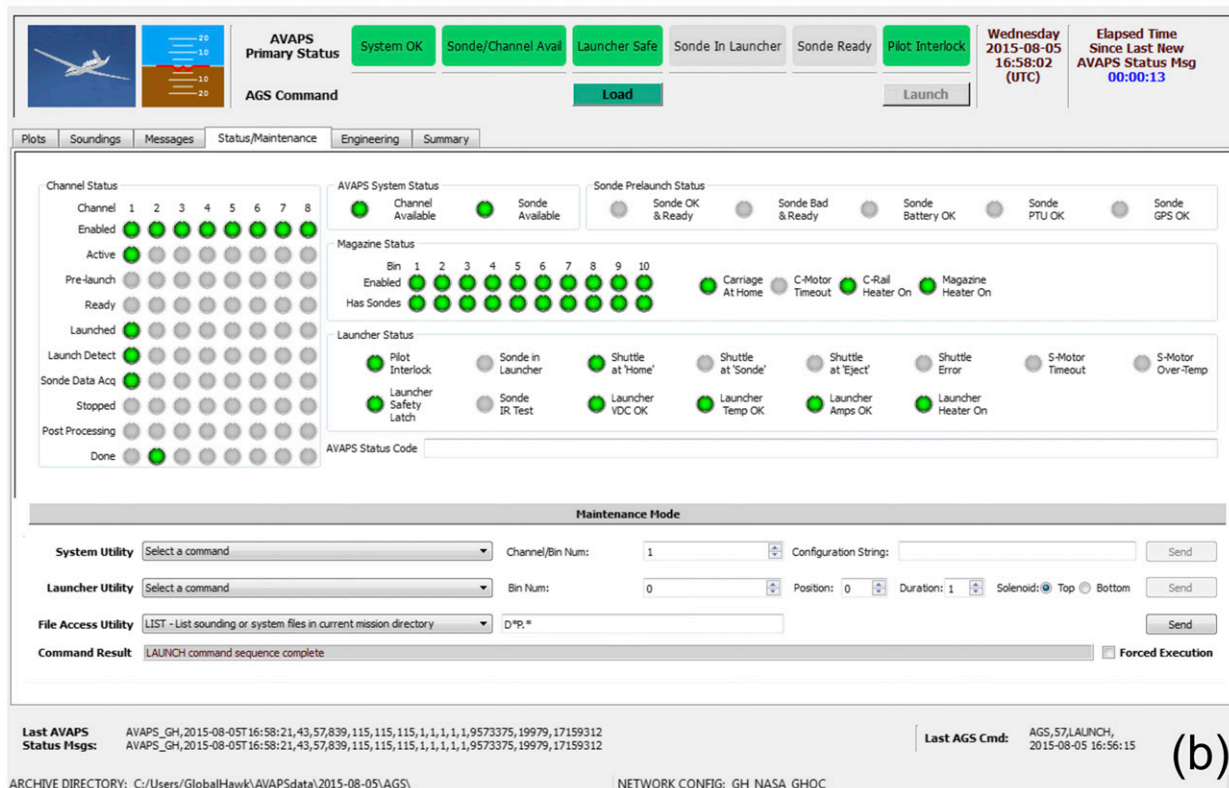
FIG. 5. Illustration of the operating controls for the GH dropsonde system as represented by screen captures from the NCAR AGS software. (a) The main and (b) status/maintenance tabs are highlighted. Additional available control screens are not shown but their function is summarized in the text.
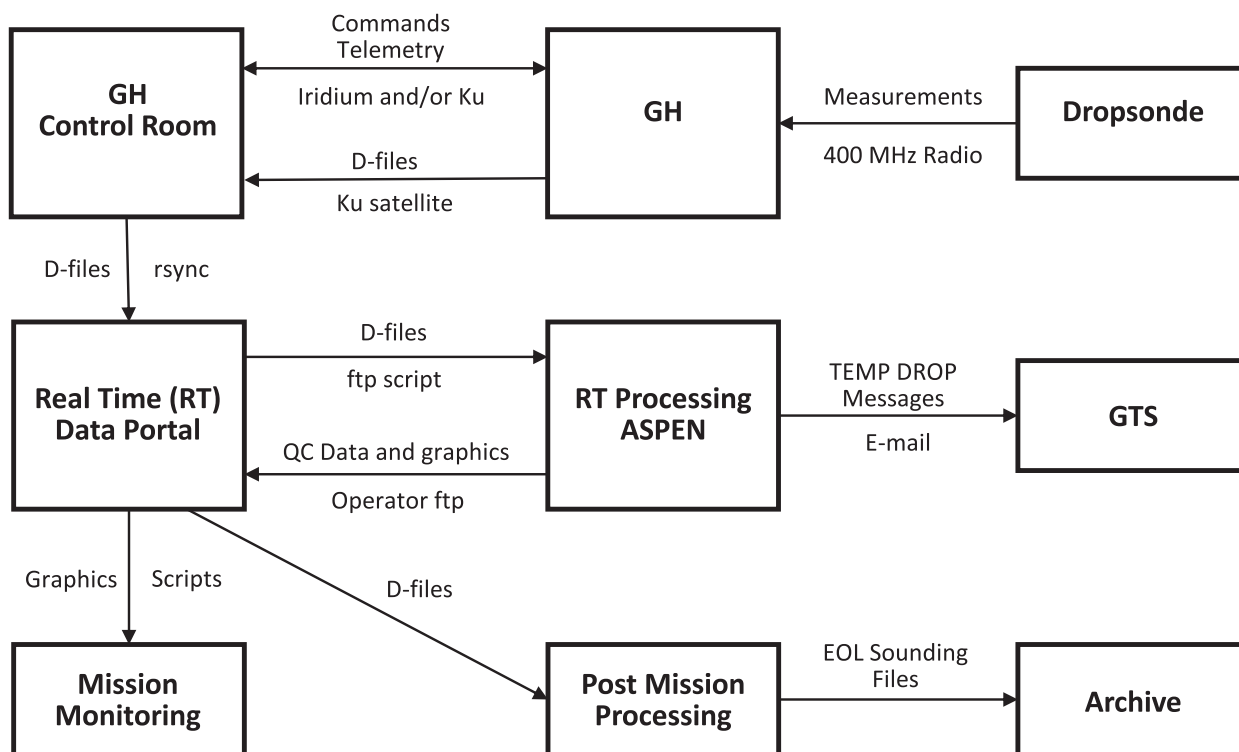
FIG. 6. Complete flow diagram for commands and data from the GH dropsonde system. Individual system elements and processing steps are represented by the rectangles, while transferred elements and the associated mechanism are highlighted by the connecting arrows. D files represent the raw sounding files. See text for further details.

and real-time display in mission monitors such as the NASA Mission Tools Suite. While ASPEN also generates full-resolution Binary Universal Form for Representation of Meteorological Data (BUFR) files, those have not, to date, been submitted through the GTS. The QC is commonly done at an off-site location to minimize staffing in the GH Operations Center. A final postmission QC is performed at a later date before data archival to provide the best possible product for research applications.

All the final quality-controlled GH dropsonde data are archived in the EOL sounding file format [see Young and Vömel (2016) for a complete description of file content and naming conventions]. The data and corresponding processing descriptions are available at EOL and also through links maintained at the NOAA Earth System Research Laboratory (https://www.esrl. noaa.gov/psd/psd2/coastal/satres/ghawk_dropsonde.html). The raw sounding files are also retained at EOL but are available only by request. Additional corrections applied during the postmission QC include a dynamic pressure correction; the dry bias correction (Vömel et al. 2016), where appropriate; a pressure calibration correction; and a refined geoid correction (see, e.g., Young and Vömel 2017). Statistics on data return are presented below in section 4a.

The operational flexibility for deployment of dropsondes from the GH has advanced significantly since the first development of the system. Necessary Federal Aviation Administration (FAA) approval for deployment of dropsondes from the unmanned GH had to be attained for the first time prior to the first campaign. Initial regulations required specification of planned drop locations 2 days in advance with limited opportunity to modify the locations in flight. Now, following substantial experience with the operation of both the NASA GH and the dropsonde system, the operational flexibility closely resembles that of manned aircraft. While notification of planned operating regions is still submitted 2 days prior to a flight, flight tracks and drop locations can be modified significantly in flight through real-time coordination with air traffic control. Since the GH flies at altitudes above traditional aircraft, in some circumstances the GH has demonstrated greater real-time flight plan flexibility than other research aircraft.

4. Campaigns and data demonstration

As of this writing, over 2700 sondes have been deployed successfully from the GH. The data are being operationally ingested in data assimilation systems and

TABLE 3. Summary of Global Hawk AVAPS dropsonde system deployments.

Experiment	Year	No. of flights	No. of sondes deployed	No. of soundings archived
WISPAR	2011	3	177	162
HS3	2011	2	80	79
	2012	6	343	337
	2013	7	433	433
	2014	11	662	656
SHOUT	2015	3	89	88
SHOUT ENRR[a]	2016	3	90	89
SHOUT HRR[b]	2016	9	648	634
EPOCH	2017	3	217	216
Total		47	2739	2694

[a] ENRR: El Niño Rapid Response.
[b] HRR: Hurricane Rapid Response.

have been utilized in several research studies. This section summarizes the missions flown thus far and highlights initial scientific observations and applications of the data.

a. Campaign and deployment summary

The GH dropsonde system has contributed valuable scientific data to four major experiments to date. A summary of the campaigns and sondes deployed is presented in Table 3. The system was first integrated during the NASA Genesis and Rapid Intensification Processes (GRIP) experiment (Braun et al. 2013) in 2010. The first GH dropsonde was launched in testing for that campaign, but a problem with the initial design of the launcher safety latch prevented system operation during the science flights. The first scientific data from the system were collected during the NOAA-led Winter Storms and Pacific Atmospheric Rivers (WISPAR) experiment in 2011 conducted from the NASA Dryden Flight Research Center (now renamed the Armstrong Flight Research Center) at Edwards Air Force Base (AFB) in California. WISPAR was conceived as an operational test of the dropsonde system but included scientific objectives related to ARs and Arctic weather (e.g., Intrieri et al. 2014).

The system was next employed during 2011–14 in the NASA Hurricane and Severe Storm Sentinel (HS3; Braun et al. 2016) project. The primary science flights exploring the formation and intensification of tropical cyclones were conducted from the NASA Wallops Flight Facility (WFF) in Virginia. The first real-time quality control and operational submission of the data through the GTS occurred during HS3. Operational assimilation of the transmitted data was also initiated at the European Centre for Medium-Range Weather Forecasts (ECMWF).

Recently, the system was deployed in the NOAA Sensing Hazards with Operational Unmanned Technology

(SHOUT) experiment in 2015–16 (Dunion et al. 2018; Wick et al. 2018) and the NASA Eastern Pacific Origins and Characteristics of Hurricanes (EPOCH) experiment in 2017. The purpose of SHOUT was to evaluate the utility of data from unmanned aircraft in improving forecasts of high-impact weather events, particularly should there ever be a gap in polar-orbiting satellite coverage. Data were operationally assimilated by NOAA for the first time in the Hurricane Weather Research and Forecasting Model (HWRF) during flights in the fall of 2015 and in the Global Forecast System (GFS) model in 2017. The observations also comprise the primary data source being evaluated in the associated ongoing data impact studies.

The data return from the GH dropsondes has generally been very good. As shown in Table 3, 98.4% of the sondes deployed from the GH have provided useful sounding data. Additional statistics on the sonde performance and data returned following QC are documented in Tables 4 and 5, respectively, for those archived soundings. The largest data quality issue was radio frequency interference (RFI) encountered on the aircraft in 2012 that prevented the successful recovery of a significant amount of sonde telemetry from lower altitudes. Since that time, however, the sondes have experienced few component failures, and the data availability has been very high. Following some early problems, the launcher performance has also been good in recent campaigns. No launcher failures occurred during 2017, and the system had a 91.2% success rate in deploying sondes planned by mission science beginning with the 2016 hurricane campaign after the last major launcher update.

b. Intercomparison with G-IV dropsondes

Two dedicated intercomparisons between dropsondes deployed from the GH and G-IV aircraft were conducted during HS3 in 2011 and 2014. While the thermodynamic and wind sensors are the same on the sondes deployed from both aircraft, subtle measurement differences could potentially result from differences in the sonde assembly, housing, and deployment. Verifying the performance of the sondes is particularly important for facilitating confident use of the data in NWP models. During both intercomparisons, sondes were deployed at common locations from both aircraft with as little time difference as possible while maintaining safe separation of the aircraft. In both experiments, collocated drops were conducted with the GH at near 18.3 km altitude and the G-IV at near 12.8 km altitude. In 2011, collocated drops were also conducted with the GH flying at 13.7 km. Both intercomparisons were conducted over the eastern Gulf of Mexico in restricted airspace west of Tampa, Florida. Average time and space separations between the drops were approximately 2 min and 5 km,

TABLE 4. Dropsonde performance statistics for archived soundings.

	All	Since 2015
Failed to transmit to surface	4.3%	1.0%
Parachute failure[a]	2.0%	0.2%
GPS failure	0.3%	0
PTU failures[b]	0.3%	0.4%

[a] Problems with the parachute leading to fast or partial fast falls of the sondes.
[b] Failures of any single components of the Vaisala sensor module.

TABLE 5. Data availability rates in final quality-controlled soundings, which is based on the percentage of seconds with valid data for each of the indicated variable types.

Variable	All soundings	Since 2015
Position	87.5%	90.4%
PTU	92.5%	94.4%
Winds	91.6%	96.6%

respectively. Conditions during the intercomparisons were fair with scattered clouds. A total of 27 collocated drops were conducted in 2011 and 15 in 2014.

While a detailed accuracy assessment is underway, an example of the composite differences between the collocated drops in 2014 is shown in Fig. 7. The results demonstrate good agreement between the measurements within expected natural atmospheric variability between the time and position of the measurements. Very small differences are observed in temperature and humidity with the GH sondes slightly warm through the depth of the troposphere and slightly moist below ~600 hPa. The wind speeds agree closely. The differences in 2011 (not shown) were generally consistent, though the GH sondes were instead slightly drier on average below ~750 hPa. Subsequent NWP usage of the GH sondes (see section 4d) has demonstrated positive forecast impacts.

c. Demonstrations in disparate meteorological settings

The quality and unique scientific utility of the GH data can be demonstrated by highlighting initial applications in diverse meteorological environments. The campaigns thus far have collected data from the Arctic atmosphere (WISPAR), over atmospheric rivers (ARs) and winter storms in the Pacific (WISPAR and SHOUT), and over tropical cyclones in the Atlantic, Caribbean, and eastern Pacific (HS3, SHOUT, and EPOCH). Samples of observations drawn from completed studies and ongoing work are presented below.

1) ARCTIC APPLICATION

Polar meteorology plays a crucial role in modulating the global weather–climate–ocean–sea ice system via energy exchange processes. Given the dearth of in situ observations in the Arctic, numerical models have typically been employed in an effort to better understand these processes. Comparisons between model output and the limited observations of key Arctic metrics such as boundary layer structures and surface fluxes, however, have generally suggested poor model performance (e.g., Tjernström et al. 2005). In parallel, Arctic sea ice is declining (e.g., Stroeve et al. 2012; Wang and Overland 2012), which can ultimately modulate extratropical weather systems and further influence the climate system (e.g., Cohen et al. 2014). Hence, better observing the Arctic environment has become a priority for atmospheric and climate scientists alike. To demonstrate the ability of the GH to collect unique observations in this sensitive region where few in situ observations exist, an Arctic flight was executed during WISPAR.

The analyses summarized below, originally included as part of a comprehensive study by Intrieri et al. (2014), are based on data collected during the flight on 9–10 March 2011 (Fig. 8). Seventy dropsondes were released during this 25-h flight, including 35 over the Arctic Ocean north of Alaska. This was the first successful GH mission with dropsonde releases at high latitudes (i.e., between 70° and 85°N).

For meteorological context, the flight track and dropsonde locations are plotted on a satellite-derived infrared (IR) image from 9 March 2011 (Fig. 8). The aircraft initially flew northwestward and transited a comma-cloud tail that approximately coincides with the location of the last of three ARs documented in the next subsection. As the GH entered the Gulf of Alaska, it turned northward and flew to within ~5° of the North Pole. The aircraft performed a triangular flight pattern over the frozen Arctic Ocean and parallel to the northern coast of Alaska before returning to Edwards AFB.

As analyzed by Intrieri et al. (2014), a set of cross-sectional analyses generated from the eight dropsondes along Alaska's northern coast (Fig. 9) highlights the ability to resolve characteristic structures over a high-latitude ice-covered region that is largely devoid of other in situ atmospheric observations. Most notable is a sharp ~15-K temperature inversion situated at or below 200 m MSL, with the deepest surface-based cold air located on the eastern half of the cross section where shallow southerly component flow was directed off the cold land surface. The inversion was shallowest on the western half of the section where westerly flow over the warmer ice-covered ocean was observed. The shallowness of the inversion here may also have been influenced
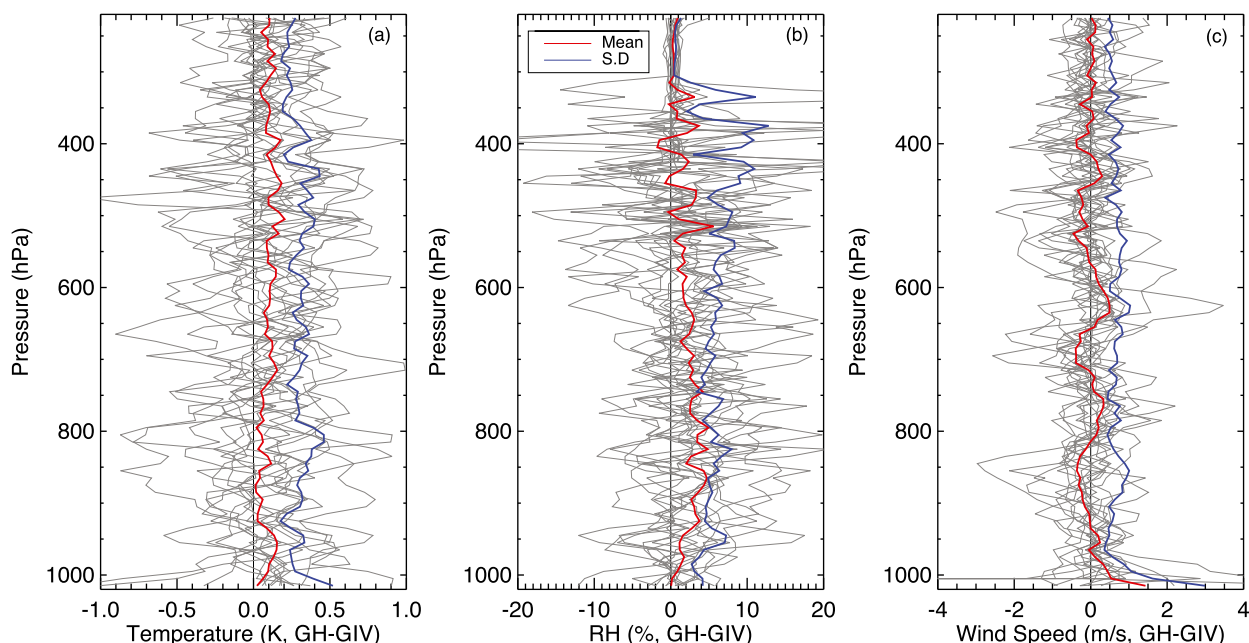
FIG. 7. Results of the intercomparison of soundings from the GH (NRD94 sondes) and NOAA G-IV (RD94 sondes) conducted over the eastern Gulf of Mexico on 30 Sep 2014. Differences are plotted for (a) temperature, (b) RH, and (c) wind speed. The differences from each of the 15 collocated soundings (gray), the mean difference (red), and the corresponding standard deviation (blue) are shown. All differences are computed as GH − G-IV as indicated. The plotted wind speed represents a combination of individual U and V components, which were similarly unbiased.

by downward mixing from a low-level westerly jet ($>12.5 \, \mathrm{m \, s^{-1}}$) observed by the three western dropsondes between 0.3 and 1.0 km MSL. Below 0.5 km MSL, the air was considerably moister in the westerly flow over the ice-covered ocean than in the southerly flow emanating from land. Interestingly, the dropsonde at 1138 UTC 10 March 2011—deployed directly above an open lead in the ocean ice at 156°W—measured a plume of moisture extending 300–400 m above the surface. These structures were not captured by satellites or models.

2) APPLICATION TO ATMOSPHERIC RIVERS

ARs are long, narrow, low-level plumes of enhanced horizontal water vapor transport (e.g., Zhu and Newell 1998; Ralph et al. 2004; Neiman et al. 2008) embedded within a broader region of generally poleward heat transport in the warm sector of maritime extratropical cyclones. Numerous publications highlight their importance in the global water cycle (Zhu and Newell 1998), heavy precipitation (e.g., Dettinger 2004; Ralph et al. 2006; Dettinger et al. 2011; Lavers et al. 2011; Neiman et al. 2008, 2011, 2013; Ralph and Dettinger 2012), snowpack (e.g., Neiman et al. 2008; Guan et al. 2012, 2013), and drought mitigation (Dettinger 2013). Given their hydrometeorological importance, scientific elements of WISPAR included targeting ARs during each

of the three GH flights. The observations highlight the unique ability of dropsondes to capture detailed measurements of water vapor transport within ARs.

Satellite- and model-based products help illustrate the meteorological conditions sampled by the GH dropsonde
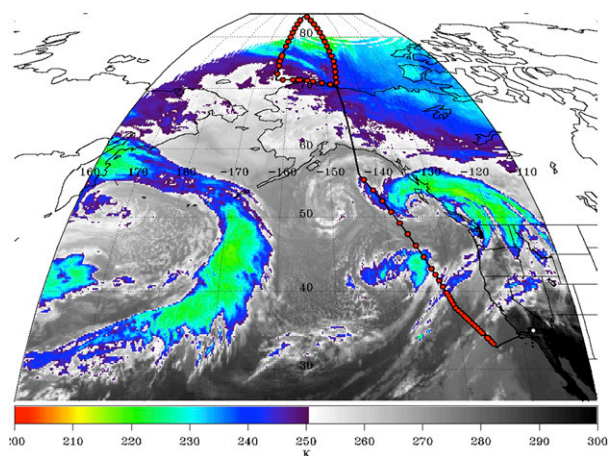

FIG. 8. *GOES-13* 10.7-μm channel infrared satellite image of brightness temperature (K; see scale) from 1800 UTC 9 Mar 2011, with the superimposed black GH flight track between 1959 UTC 9 Mar and 2101 UTC 10 Mar 2011. Dropsonde locations (red dots along the flight track) and the location of Edwards AFB (white dot) are marked. An AR cloud band is seen impacting the U.S. West Coast along the Oregon–Washington border and extending southwestward offshore.

observations. Retrievals of integrated water vapor (IWV) were generated following Wentz (1995) based on Special Sensor Microwave Imager/Sounder (SSMIS; Kunkee et al. 2008) observations. Plan-view analyses of vertically integrated horizontal water vapor transport (IVT) were generated (methodology as in Neiman et al. 2008) from the Climate Forecast System Reanalysis (CFSR) global gridded dataset (Saha et al. 2010).

Figure 10 places the three AR-related flights into synoptic-scale perspective and highlights the locations of the dropsonde cross sections in Figs. 11 and 12. The first flight targeted the subtropical segment of an AR plume of enhanced IWV and IVT extending from near Hawaii to the Pacific Northwest (Figs. 10a,d). During AR landfall, moderate precipitation ($\sim$50–100 mm) fell in Washington's Olympic Mountains. The second mission flew through the poleward terminus of an AR that became entrained in a midlatitude cyclogenesis event offshore of British Columbia (Figs. 10b,e). Although IWV was modest in this portion of the AR, IVT was considerable, thus revealing that strong winds contributed significantly to the observed vapor fluxes. Approximately 40–80 mm of precipitation fell in California's northern coastal mountains and Sierra Nevada during this event. Last, the outbound leg of the Arctic flight (see the previous subsection) transected a midlatitude AR impacting the U.S. West Coast (Figs. 10c,f), when as much as 100 mm of precipitation fell across the coastal mountains of Oregon and Washington. The IWV plume associated with the AR extended from Hawaii to the Pacific Northwest, while the associated IVT plume was confined to the mid-latitudes in advance of a landfalling extratropical cyclone.

Figure 11 shows cross-sectional analyses of AR-parallel isotachs with water vapor specific humidity (U and q, respectively, left column) and water vapor transport (right column) across the ARs described above. The cross section from the first flight (Figs. 11a,d) transected a subtropical segment of the AR where IWV exceeded 4 cm near the southern terminus of the strong IVT plume (Figs. 10a,d). The atmospheric structures contained in this cross section mirror those found in two previously published subtropical ARs observed with NOAA research aircraft (Ralph et al. 2011; Neiman et al. 2014), including strong northeastward-directed water vapor fluxes (80–100 kg s^{-1} m^{-1}) in the core of the AR on the warm side of a cold front. The cross-sectional baselines during the flights of 3–4 March (Figs. 11b,e) and 9–10 March (Figs. 11c,f) transected ARs in the midlatitudes offshore of California (Figs. 10b,e, 10c,f). Unlike the first published midlatitude AR cross section analyzed using dropsondes released from the lower-flying NOAA P-3 (Ralph et al. 2004), the GH cross sections each capture an AR in the context of the full-tropospheric polar jet front system. In both cases, vapor fluxes > 50 kg s^{-1} m^{-1} in the
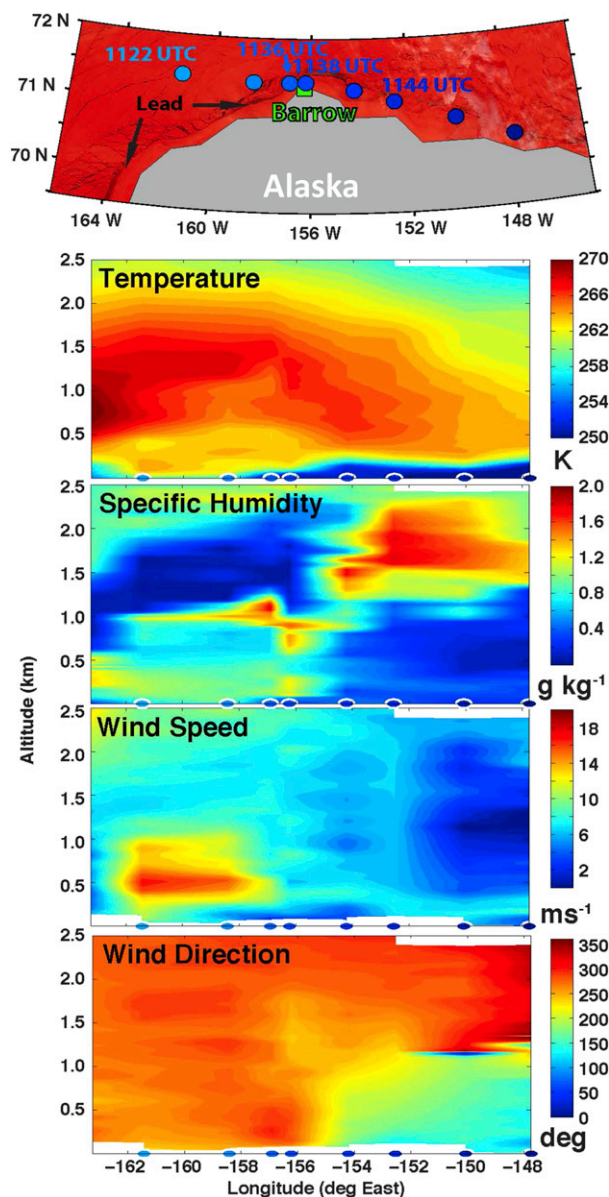

FIG. 9. (top) Plan-view perspective of eight dropsondes (blue dots) released from the GH between 1122 and 1157 UTC 10 Mar 2011 along Alaska's northern coast. A background satellite image with 500-m horizontal resolution from the Moderate Resolution Imaging Spectroradiometer (MODIS) at 1030 UTC 10 Mar 2011 is also shown, with larger ice leads or breaks in the ice visible as darker shading highlighted. (top to bottom) Dropsonde cross sections of temperature (K), specific humidity (g kg^{-1}), wind speed (m s^{-1}), and wind direction ($^\circ$). Dropsonde locations are marked (blue dots), as in the top panel. This figure originally appeared as Fig. 5 in Intrieri et al. (2014) and is used with permission.

AR are situated largely on the warm side of a polar cold front that extends upward to the cyclonic shear side of a $\sim$65 m s^{-1} polar jet near the tropopause. Although the magnitude and vertical extent of the AR vapor fluxes in
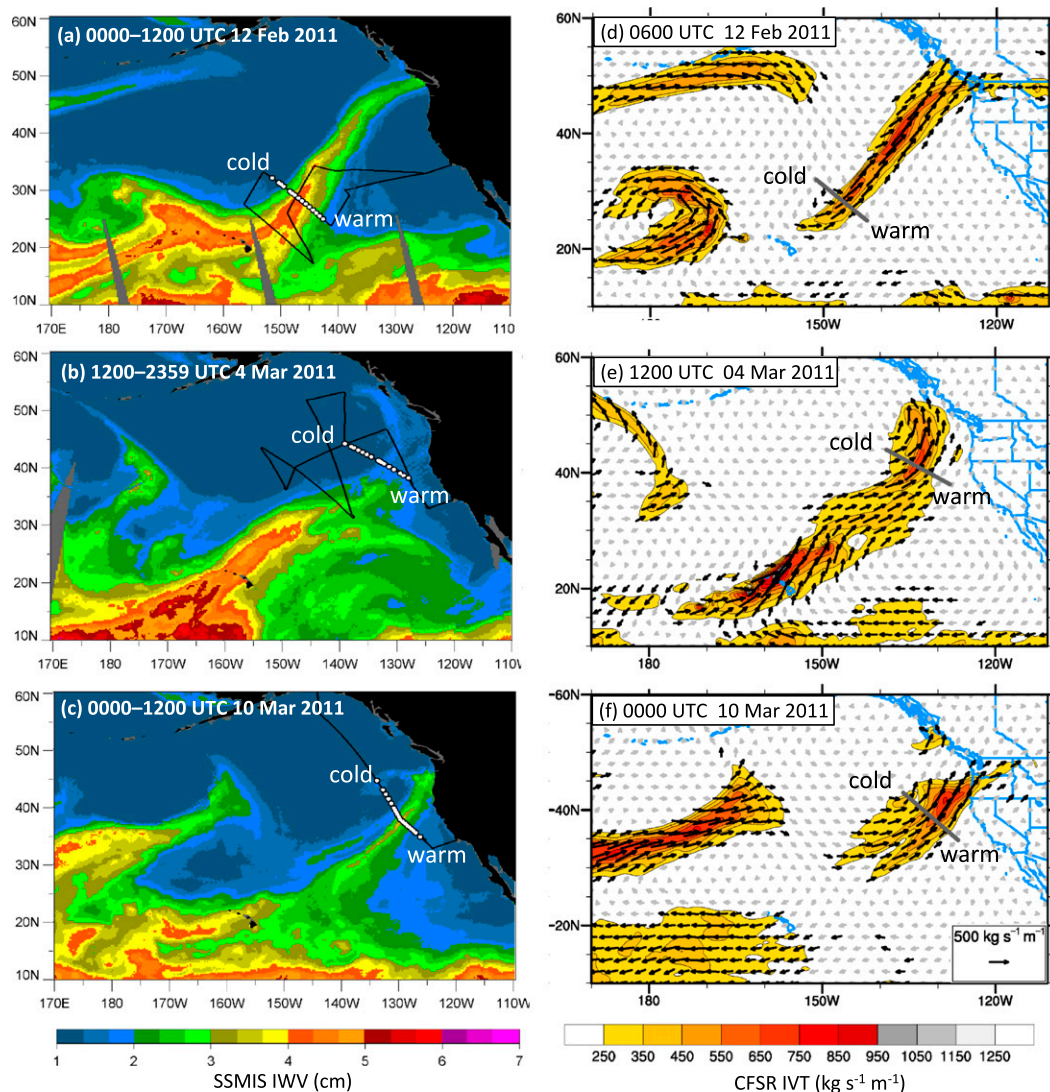
FIG. 10. (left) Composite SSMIS satellite imagery of IWV (cm; color scale at bottom) constructed from polar-orbiting swaths on (a) 0000–1200 UTC 12 Feb 2011, (b) 1200–2359 UTC 4 Mar 2011, and (c) 0000–1200 UTC 10 Mar 2011. The GH flight track within each domain is marked (thin line). The white dots superimposed on the corresponding lines show the locations of the dropsondes used in the cross sections shown in Fig. 11. (right) The 1000–200-hPa IVT (kg s^{-1} m^{-1}; color scale at bottom) constructed from the CFSR dataset at (d) 0600 UTC 12 Feb 2011, (e) 1200 UTC 4 Mar 2011, and (f) 0000 UTC 10 Mar 2011. IVT vectors are overlaid [length scale shown in (f); dark vectors > 250 kg s^{-1} m^{-1}]. The bold lines labeled "cold" and "warm" in the top/middle/bottom rows mark the cross-sectional projections for the corresponding top/middle/bottom rows of Fig. 11.

the midlatitude cross sections mirror those in the subtropical cross section, significant structural differences exist: (i) the southwesterly flow is stronger but drier in the midlatitude cross sections and (ii) the width of IVT > 250 kg s^{-1} m^{-1} is almost twice as wide in the midlatitude cross sections, and, consequently, it shows total vapor transport in this core region that is 50%–70% stronger than its subtropical counterpart.

The dropsonde observations, particularly of IVT, reveal key information on AR structure not available from satellite observations. While IWV retrievals provide a visual indication of potential AR position, they do not fully reflect the fundamental transport characteristics of ARs, and the data, lacking profile information, are of limited value for data assimilation. The dropsonde cross sections (Fig. 12) demonstrate how the AR-parallel IVT (Fig. 12b) reveals a much sharper AR signature than the corresponding IWV. For these three cases, the maximum values of IVT are within 18% of each other, while the maximum value of IWV varies by a factor of ~2.5.
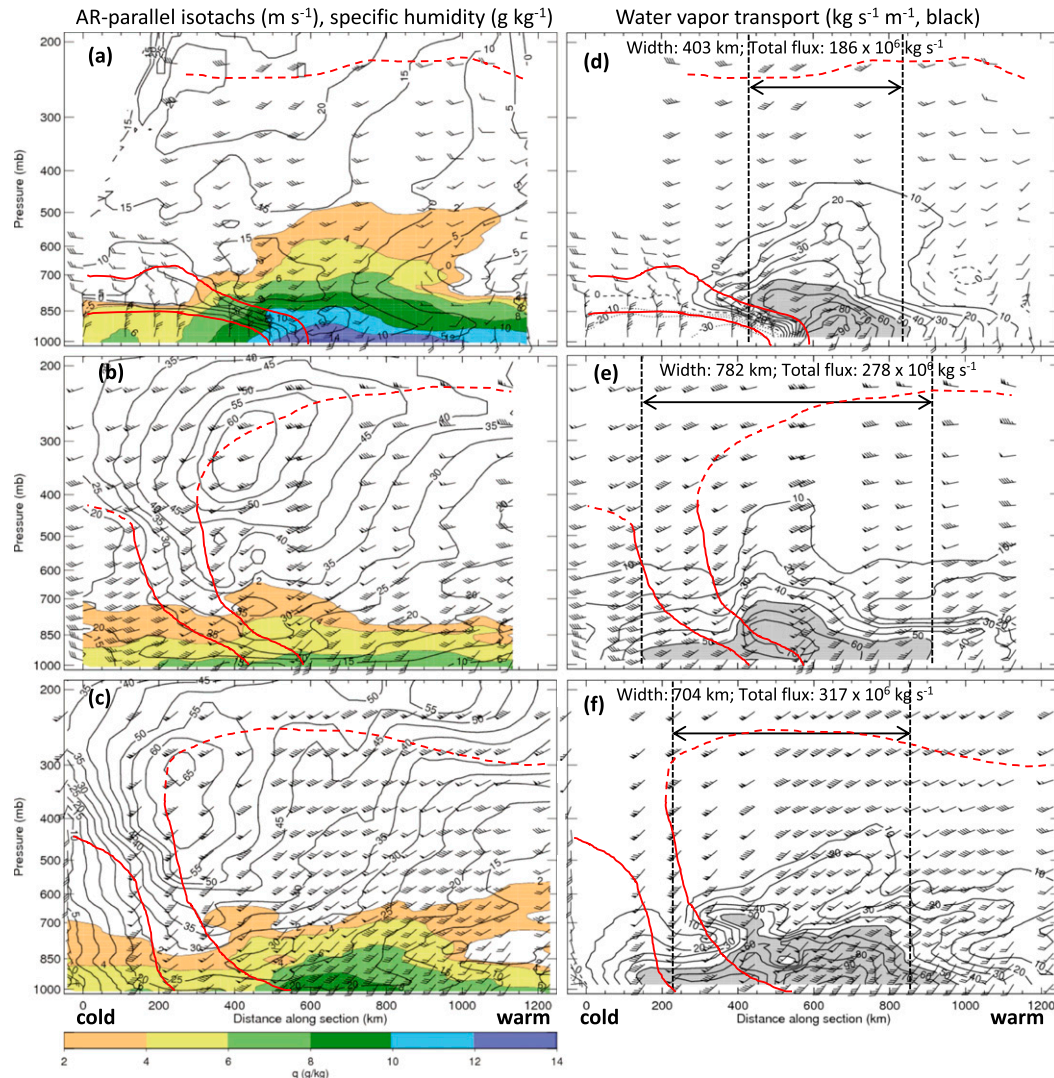
FIG. 11. (left) Cross sections of AR-parallel horizontal isotachs (m s^{-1}; black solid contours) and water vapor specific humidity (g kg^{-1}; color shaded) at (a) 0536–0726 UTC 12 Feb 2011 (left to right, respectively) along baseline "cold–warm" in Fig. 10d, with isotachs directed from 235°; (b) 1102–1416 UTC 4 Mar 2011 (left to right, respectively) along baseline cold–warm in Fig. 10e, with isotachs directed from 235°; and (c) 2219 UTC 9 Mar–0022 UTC 10 Mar 2011 (right to left, respectively) along baseline cold–warm in Fig. 10f, with isotachs directed from 230°. The best estimates of the polar cold frontal boundaries (solid red) and tropopause (dashed red) based on these analyses and on companion analyses of potential temperature and equivalent potential temperature (not shown). Wind flags = 25 m s^{-1}, barbs = 5 m s^{-1}, and half barbs = 2.5 m s^{-1}. (right) As in the left column, except for AR-parallel horizontal water vapor flux (kg s^{-1} m^{-1}; black contours; shading: >50 kg s^{-1} m^{-1}). The pairs of vertical black dashed lines enclose IVT > 250 kg s^{-1} m^{-1}; the width and total flux within each pair of dashed lines are shown.

Similar results highlighting the utility of using aircraft-derived IVT in identifying ARs were also demonstrated by Ralph et al. (2017).

3) TROPICAL APPLICATION: HURRICANE EDOUARD

Tropical cyclone research and monitoring are important applications for long-endurance unmanned aircraft like the GH. The science of HS3 was designed around the GH capabilities and a major focus of the SHOUT project was evaluating the utility of GH observations for improving forecasts of high-impact weather events like hurricanes. This subsection highlights the ability of dropsonde observations from the GH to capture unique high-resolution observations of tropical cyclone storm structure with greater vertical and horizontal extent than possible from other current conventional platforms.
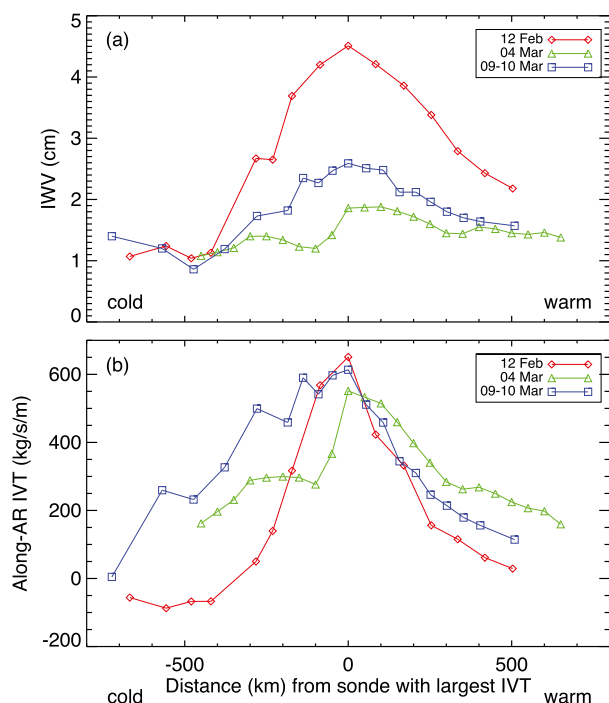
FIG. 12. (a) Traces of 1000–200-hPa IWV (cm) for the three cross sections in Fig. 11 (see key). The traces are centered on the maximum value of IWV. (b) As in (a), except for AR-parallel IVT (kg s^{-1} m^{-1}).

Hurricane Edouard from 2014 initially tracked northwestward away from the west coast of North Africa and subsequently arced clockwise around a subtropical ridge. It attained hurricane status on 14 September, reached peak wind intensity of ~52 m s^{-1} with a minimum central pressure of 955 hPa on 16 September when the GH was airborne, and subsequently weakened by 19 September west of the Azores. During a mission on 16–17 September, the GH conducted eight radial transects across Edouard's center, releasing 87 dropsondes into the hurricane environment. The flight, which approximately coincided with the storm's peak intensity, captured the strongest hurricane conditions directly sampled with GH dropsondes to date.

Geosynchronous IR satellite observations of Edouard with locations of temporally relevant dropsondes are presented at two times (Figs. 13a,b). To show the dropsondes in proper spatial context relative to the moving hurricane, we spatially adjusted the dropsonde positions to the times of the imagery by applying Taylor's (1938) hypothesis, which assumes that large-scale conditions are steady-state and propagate at a fixed phase velocity. A hurricane phase velocity was determined for each panel in Fig. 13 by estimating the translational motion of the hurricane's eye using sequential 30-min satellite imagery. For the earlier satellite-image time, a hurricane phase

velocity of 6.4 m s^{-1} from 187.4° was calculated and then used to spatially adjust the dropsondes comprising the first three radial flight legs. For the later time, a velocity of 8.3 m s^{-1} from 212.8° was used to spatially adjust the dropsondes comprising radial flight legs 4–7. All spatial adjustments were solely based on the dropsonde launch location. In both panels, 800-hPa wind speeds of >20 m s^{-1} encircled Edouard, with hurricane-force flow of ~35–45 m s^{-1} confined to a tight radius around the distinctive ~30-km-wide eye. The strongest winds occupied the southern and eastern quadrants, consistent with storm motion from the south-southwest. The results demonstrate that the GH was successful sampling the storm center with multiple passes.

A wind and thermodynamic analysis of Edouard is provided in an east–west cross section composed of 10 dropsondes released during a flight leg between 2336 UTC 16 September and 0123 UTC 17 September 2014 and spatially adjusted following the methodology described in the previous paragraph (Figs. 14a,b; white baseline in Fig. 13b). Because none of these dropsondes were situated in the hurricane's eye, an eleventh dropsonde released within the eye at 2214 UTC 16 September (~1.25 h prior to the first dropsonde launch in the section) was also included in the analysis. Strong winds exhibited asymmetric characteristics about the weak flow in the eye (Fig. 14a). Namely, southerly flow exceeding 25 m s^{-1} extended eastward from the eye for 300 km and reached upward to 400 hPa, and maximum southerly flow of >50 m s^{-1} was situated at 750 hPa. In contrast, west of the eye northerly flow in excess of 25 m s^{-1} was confined to a 200-km radius and below 600 hPa, while maximum northerly winds of only 35 m s^{-1} remained shallow (i.e., ~900 hPa). These results are again consistent with a storm motion from the south-southwest. A companion analysis of specific humidity (Fig. 14a) shows a 150-km radius of enhanced water vapor up to at least 400 hPa, with maximum values of 18–21 g kg^{-1} in the eye below 850 hPa. A cross section of equivalent potential temperature (θ_e; Fig. 14b, computed following Bolton 1980) captures moist-neutral stability in the 100-km-radius eyewall region through the depth of the troposphere and values of $\theta_e > 345$ K in this region. The eye proper was characterized by θ_e ranging from 355 to 362 K. The corresponding analysis of relative humidity (Fig. 14b) shows essentially saturated conditions within 150 km of the eye from the surface to ~450 hPa. Dry air on the eastern side of the hurricane is evident and is consistent with less cloudiness east of the storm (Fig. 13). A companion dropsonde trace of IWV through the hurricane (Fig. 14c) shows a peak value of almost 8 cm near the center, with IWV diminishing to <5 cm away from the storm. The corresponding IWV trace obtained from the SSMIS IWV satellite image at 2315 UTC
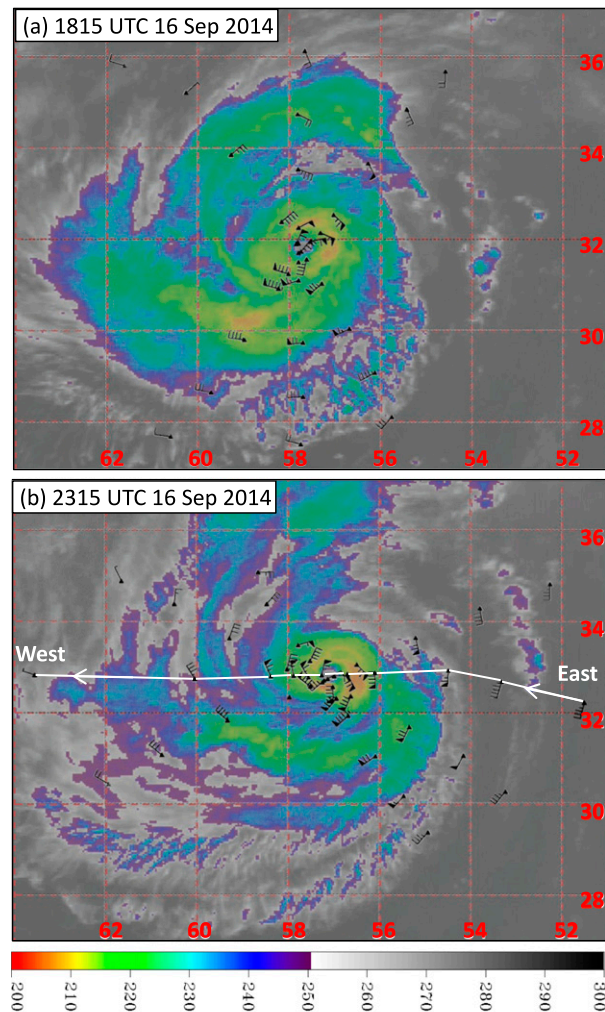
FIG. 13. *GOES-13* 10.7-μm channel IR satellite images of brightness temperature (K; see scale) centered on Hurricane Edouard at (a) 1815 UTC 16 Sep and (b) 2315 UTC 16 Sep 2014. The following spatially adjusted GH dropsonde wind velocities (see text for details) at 800 hPa are shown on the satellite images: (a) radial flight legs 1–3 between 1507 and 2055 UTC 16 Sep 2014, and (b) radial flight legs 4–7 between 2121 UTC 16 Sep and 0502 UTC 17 Sep 2014. Wind flags and barbs are as in Fig. 11. The line in (b), with endpoint labels "west" and "east," mark the cross section shown in Fig. 14.

to deploy dropsondes from above the cyclones, in their ability to sample the full vertical storm extent in detail into the lower stratosphere. Observations from aircraft like the P-3 and C-130 typically sample only the lower portion of these storms, while the higher-flying G-IV is unable to safely fly over their tops and instead usually samples the surrounding environment.

d. Operational impact

The GH dropsonde data are increasingly being seen to have tremendous potential value for operational forecasting of high-impact weather. The GH dropsonde data have been successfully assimilated operationally in ECMWF's data assimilation system since September 2011. Tropical cyclone observations collected during SHOUT were used in real time by forecasters at the National Hurricane Center and cited in 10 forecast discussions spanning the four distinct systems sampled in 2016. Even more significantly, studies conducted by the Environmental Modeling Center (EMC) at the National Centers for Environmental Prediction (NCEP) with the SHOUT data demonstrated that the observations could lead to improvements in the accuracy of tropical cyclone track forecasts within the GFS model of up to 13% at 72-h lead time and in the intensity forecasts within the HWRF of up to 14% at the same lead time (Wick et al. 2018). A complete analysis of these results, including extension to the observations from 2017, is being prepared for publication by scientists at EMC.

5. Conclusions

A new dropsonde system building on proven NCAR AVAPS technology was developed for the GH unmanned aircraft and demonstrated in multiple scientific campaigns. The system supports eight simultaneous soundings and can carry up to 90 of the miniaturized dropsondes. The GH enables deployment of the sondes from altitudes up to 19.8 km and above hazardous weather during flights with durations in excess of 24 h. Over 2700 sondes have been successfully deployed to date during four major campaigns. The system is controlled by an operator on the ground in coordination with the mission scientists and aircraft pilots. A comprehensive data management framework has been established enabling real-time access to and quality control of the data for operational and research applications.

Data collected by the system has been employed in real time by hurricane forecasters and for assimilation into NWP models as well as in numerous postmission scientific analyses spanning diverse meteorological environments. While many of the analyses are still ongoing, the unique capabilities and sampling provided by the system
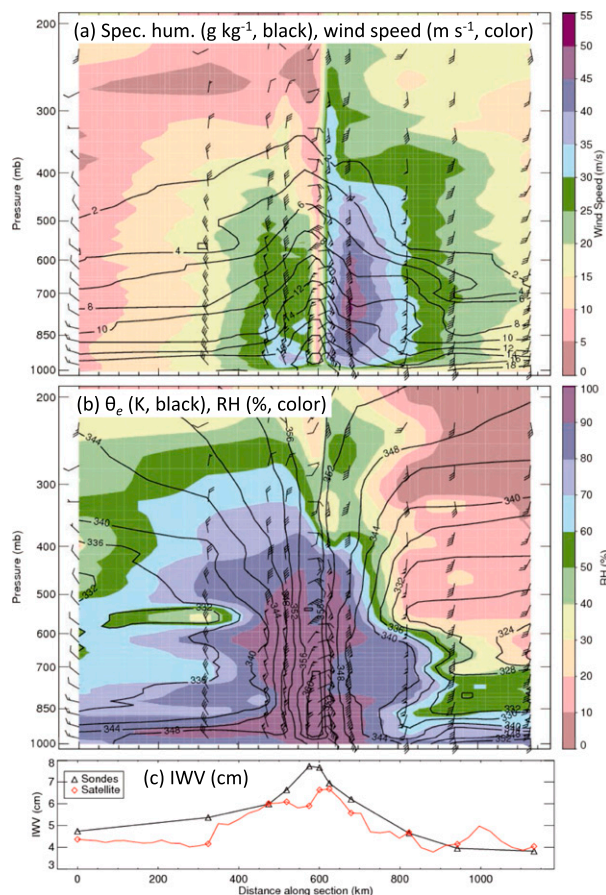
16 September (the same time as the satellite image in Fig. 13b) compares relatively poorly, especially in the eyewall region where heavy convective precipitation is typically observed. The heavy rain likely degraded the SSMIS IWV retrievals as a result of the microwave emission from large droplets, thus pointing to the value-added information from the dropsondes.

The GH observations are unique not only in their ability to capture continuous tropical cyclone evolution over extended flights but also, given the aircraft's ability

FIG. 14. Spatially adjusted GH dropsonde cross-sectional analyses through Hurricane Edouard along baseline west–east in Fig. 13b at 2315 UTC 16 Sep 2014: (a) water vapor specific humidity (g kg^{-1}; black contours) and total horizontal wind speed (m s^{-1}; color filled); (b) equivalent potential temperature (θ_e, K; black contours) and RH (%; color filled); and (c) IWV (cm) from the dropsondes (black) and corresponding SSMIS IWV satellite image at 2315 UTC 16 Sep (red; all pixels along the baseline are included). Wind flags and barbs in (a) and (b) are as in Fig. 11. Dropsondes from 2336 UTC 16 Sep to 0123 UTC 17 Sep 2014 are shown (time increases leftward, except for the earlier dropsonde within the eye at 2214 UTC 16 Sep), and the distance (km) along the cross section is indicated at the bottom.

are evident. The observations enable detailed high-vertical-resolution measurements throughout a large fraction of the atmospheric column, resolving structures not apparent through other existing observing systems. Recent results emerging from studies examining the effect on GH dropsondes deployed during the 2016 SHOUT hurricane campaign are suggesting notable positive impacts on forecasts of hurricane track and intensity. A comprehensive assessment of the overall accuracy of dropsonde data from both the GH and other manned aircraft is being completed separately. Two dedicated intercomparisons with collocated drops from a

manned aircraft, however, have demonstrated comparable performance of the GH measurements as expected given the similarity of the sensors.

Through the multiple deployments, the system has attained a high level of maturity and it is essentially ready for operational utilization should the GH be employed in that manner for extreme weather warning and forecasting. Fielding a fully operational system for future GH missions should be possible through relatively minor refinements to the existing design. A derivative of the GH dropsonde launcher has also been developed by NCAR and is in use on the NSF–NCAR Gulfstream V aircraft.

REFERENCES

Bolton, D., 1980: Computation of equivalent potential temperature. *Mon. Wea. Rev.*, **108**, 1046–1053, https://doi.org/10.1175/1520-0493(1980)108<1046:TCOEPT>2.0.CO;2.

Braun, S. A., and Coauthors, 2013: NASA's Genesis and Rapid Intensification Processes (GRIP) field experiment. *Bull. Amer. Meteor. Soc.*, **94**, 345–363, https://doi.org/10.1175/BAMS-D-11-00232.1.

——, P. A. Newman, and G. M. Heymsfield, 2016: NASA's Hurricane and Severe Storm Sentinel (HS3) investigation. *Bull. Amer. Meteor. Soc.*, **97**, 2085–2102, https://doi.org/10.1175/BAMS-D-15-00186.1.

Cohen, J., and Coauthors, 2014: Recent Arctic amplification and extreme mid-latitude weather. *Nat. Geosci.*, **7**, 627–637, https://doi.org/10.1038/ngeo2234.

Cohn, S. A., and Coauthors, 2013: Driftsondes: Providing in situ long-duration dropsonde observations over remote regions. *Bull. Amer. Meteor. Soc.*, **94**, 1661–1674, https://doi.org/10.1175/BAMS-D-12-00075.1.

Cole, H. L., S. Rossby, and P. K. Govind, 1973: The NCAR wind-finding dropsonde. *Atmos. Technol.*, **2**, 19–24.

Dettinger, M. D., 2004: Fifty-two years of ''pineapple-express'' storms across the west coast of North America. California Climate Change Center Rep. Series 2005-003, USGS, Scripps Institution of Oceanography for the California Energy Commission, PIER Project Rep., CEC-500-2005-004, http://www.energy.ca.gov/2005publications/CEC-500-2005-004/CEC-500-2005-004.PDF, 15 pp.

——, 2013: Atmospheric rivers as drought busters on the U.S. West Coast. *J. Hydrometeor.*, **14**, 1721–1732, https://doi.org/10.1175/JHM-D-13-02.1.

——, F. M. Ralph, T. Das, P. J. Neiman, and D. Cayan, 2011: Atmospheric rivers, floods, and the water resources of California. *Water*, **3**, 445–478, https://doi.org/10.3390/w3020445.

Dunion, J. P., G. A. Wick, P. G. Black, and J. Walker, 2018: Sensing hazards with operational unmanned technology: 2015–2016 campaign summary, final report. NOAA Tech. Memo. OAR UAS-001, 39 pp.

Franklin, J. L., M. L. Black, and K. Valde, 2003: GPS dropwindsonde wind profiles in hurricanes and their operational implications. *Wea. Forecasting*, **18**, 32–44, https://doi.org/10.1175/1520-0434(2003)018<0032:GDWPIH>2.0.CO;2.

Gelaro, R., R. H. Langland, S. Pellerin, and R. Todling, 2010: The THORPEX observation impact intercomparison experiment. *Mon. Wea. Rev.*, **138**, 4009–4025, https://doi.org/10.1175/2010MWR3393.1.

Guan, B., D. E. Waliser, N. P. Molotch, E. J. Fetzer, and P. J. Neiman, 2012: Does the Madden–Julian oscillation influence wintertime atmospheric rivers and snowpack in the Sierra Nevada? *Mon. Wea. Rev.*, **140**, 325–342, https://doi.org/10.1175/MWR-D-11-00087.1.

——, N. P. Molotch, D. E. Waliser, E. J. Fetzer, and P. J. Neiman, 2013: The 2010/11 snow season in California's Sierra Nevada: Role of atmospheric rivers and modes of large-scale variability. *Water Resour. Res.*, **49**, 6731–6743, https://doi.org/10.1002/wrcr.20537.

Hock, T. F., and H. L. Cole, 1991: A new aircraft universal lightweight digital dropwindsonde. Preprints, *Seventh Symp. on Meteorological Observations and Instrumentation*, New Orleans, LA, Amer. Meteor. Soc., 291–296.

——, and J. L. Franklin, 1999: The NCAR GPS dropwindsonde. *Bull. Amer. Meteor. Soc.*, **80**, 407–420, https://doi.org/10.1175/1520-0477(1999)080<0407:TNGD>2.0.CO;2.

Intrieri, J. M., and Coauthors, 2014: Global Hawk dropsonde observations of the Arctic atmosphere obtained during the Winter Storms and Pacific Atmospheric Rivers (WISPAR) field campaign. *Atmos. Meas. Tech.*, **7**, 3917–3926, https://doi.org/10.5194/amt-7-3917-2014.

Jensen, E. J., and Coauthors, 2017: The NASA Airborne Tropical Tropopause Experiment: High-altitude aircraft measurements in the tropical western Pacific. *Bull. Amer. Meteor. Soc.*, **98**, 129–143, https://doi.org/10.1175/BAMS-D-14-00263.1.

Kunkee, D., G. A. Poe, D. Boucher, S. Swadley, Y. Hong, J. Wessel, and E. Uliana, 2008: Design and evaluation of the first Special Sensor Microwave Imager/Sounder (SSMIS). *IEEE Trans. Geosci. Remote Sens.*, **46**, 863–883, https://doi.org/10.1109/TGRS.2008.917980.

Lavers, D. A., R. P. Allan, E. F. Wood, G. Villarini, D. J. Brayshaw, and A. J. Wade, 2011: Winter floods in Britain are connected with atmospheric rivers. *Geophys. Res. Lett.*, **38**, L23803, https://doi.org/10.1029/2011GL049783.

Neiman, P. J., F. M. Ralph, G. A. Wick, J. Lundquist, and M. D. Dettinger, 2008: Meteorological characteristics and overland precipitation impacts of atmospheric rivers affecting the West Coast of North America based on eight years of SSM/I satellite observations. *J. Hydrometeor.*, **9**, 22–47, https://doi.org/10.1175/2007JHM855.1.

——, L. J. Schick, F. M. Ralph, M. Hughes, and G. A. Wick, 2011: Flooding in western Washington: The connection to atmospheric rivers. *J. Hydrometeor.*, **12**, 1337–1358, https://doi.org/10.1175/2011JHM1358.1.

——, F. M. Ralph, B. J. Moore, M. Hughes, K. M. Mahoney, J. Cordeira, and M. D. Dettinger, 2013: The landfall and inland penetration of a flood-producing atmospheric river in Arizona. Part I: Observed synoptic-scale, orographic, and hydrometeorological characteristics. *J. Hydrometeor.*, **14**, 460–484, https://doi.org/10.1175/JHM-D-12-0101.1.

——, G. A. Wick, B. J. Moore, F. M. Ralph, J. R. Spackman, and B. Ward, 2014: An airborne study of an atmospheric river over the subtropical pacific during WISPAR: Dropsonde budget-box diagnostics, and precipitation impacts in Hawaii. *Mon. Wea. Rev.*, **142**, 3199–3223, https://doi.org/10.1175/MWR-D-13-00383.1.

Ota, Y., J. C. Derber, E. Kalnay, and T. Miyoshi, 2013: Ensemble-based observation impact estimates using the NCEP GFS. *Tellus*, **65A**, 20 038, https://doi.org/10.3402/tellusa.v65i0.20038.

Ralph, F. M., and M. D. Dettinger, 2012: Historical and national perspectives on extreme West Coast precipitation associated with atmospheric rivers during December 2010. *Bull. Amer. Meteor. Soc.*, **93**, 783–790, https://doi.org/10.1175/BAMS-D-11-00188.1.

——, P. J. Neiman, and G. A. Wick, 2004: Satellite and CALJET aircraft observations of atmospheric rivers over the eastern North Pacific Ocean during the winter of 1997/98. *Mon. Wea. Rev.*, **132**, 1721–1745, https://doi.org/10.1175/1520-0493(2004)132<1721:SACAOO>2.0.CO;2.

——, ——, ——, S. I. Gutman, M. D. Dettinger, D. R. Cayan, and A. B. White, 2006: Flooding on California's Russian River: The role of atmospheric rivers. *Geophys. Res. Lett.*, **33**, L13801, https://doi.org/10.1029/2006GL026689.

——, ——, G. N. Kiladis, K. Weickmann, and D. M. Reynolds, 2011: A multiscale observational case study of a Pacific atmospheric river exhibiting tropical–extratropical connections and a mesoscale frontal wave. *Mon. Wea. Rev.*, **139**, 1169–1189, https://doi.org/10.1175/2010MWR3596.1.

——, and Coauthors, 2017: Dropsonde observations of water vapor transport within North Pacific atmospheric rivers. *J. Hydrometeor.*, **18**, 2577–2596, https://doi.org/10.1175/JHM-D-17-0036.1.

Saha, S., and Coauthors, 2010: The NCEP Climate Forecast System Reanalysis. *Bull. Amer. Meteor. Soc.*, **91**, 1015–1057, https://doi.org/10.1175/2010BAMS3001.1.

Stroeve, J. C., M. C. Serreze, M. M. Holland, J. E. Kay, J. Maslanik, and A. P. Barrett, 2012: The Arctic's rapidly shrinking sea ice cover: A research synthesis. *Climatic Change*, **110**, 1005–1027, https://doi.org/10.1007/s10584-011-0101-1.

Taylor, G. I., 1938: The spectrum of turbulence. *Proc. Roy. Soc. London*, **164A**, 476–490, https://doi.org/10.1098/rspa.1938.0032.

Tjernström, M., and Coauthors, 2005: Modeling the Arctic boundary layer: An evaluation of six ARCMIP regional-scale models using data from the SHEBA project. *Bound.-Layer Meteor.*, **117**, 337–381, https://doi.org/10.1007/s10546-004-7954-z.

Vaisala, 2016: Vaisala dropsonde RD94. Data Sheet, 2 pp., https://www.vaisala.com/sites/default/files/documents/RD94-Datasheet-B210936EN-B.pdf.

Vömel, H., K. Young, and T. Hock, 2016: NCAR GPS dropsonde humidity dry bias. NCAR Tech. Note NCAR/TN-531+STR, 7 pp., http://dx.doi.org/10.5065/D6XS5SGX.

Wang, M., and J. E. Overland, 2012: A sea ice free summer Arctic within 30 years: An update from CMIP5 models. *Geophys. Res. Lett.*, **39**, L18501, https://doi.org/10.1029/2012GL052868.

Wentz, F. J., 1995: The intercomparison of 53 SSM/I water vapor algorithms. Remote Sensing Systems Tech. Rep., 19 pp.

Wick, G. A., J. P. Dunion, and J. Walker, 2018: Sensing hazards with operational unmanned technology: Impact study of Global Hawk unmanned aircraft system observations for hurricane forecasting, final report. NOAA Tech. Memo. OAR UAS-002, 73 pp., http://dx.doi.org/10.7289/V5/TM-OAR-UAS-002.

Young, K. and H. Vömel, 2016: EOL sounding file format. UCAR Earth Observing Laboratory, 3 pp., https://www.eol.ucar.edu/system/files/files/observing_facility/AVAPS%20Dropsonde%20System/v4.EOL%20Sounding%20Data%20File%20Format.docx.

——, and ——, 2017: SHOUT-HRR dropsonde data quality report. NCAR Rep., 10 pp., http://data.eol.ucar.edu/datafile/nph-get/517.003/readme.SHOUT2016-HRR.GH-Dropsondes.pdf.

Zhu, Y., and R. E. Newell, 1998: A proposed algorithm for moisture fluxes from atmospheric rivers. *Mon. Wea. Rev.*, **126**, 725–735, https://doi.org/10.1175/1520-0493(1998)126<0725:APAFMF>2.0.CO;2.